1 Nanoscale X-ray detectors based on individual CdS, SnO$_2$ and ZnO
2 nanowires

3

4   *Edgars Butanovs[*], Aleksejs Zolotarjovs, Alexei Kuzmin, Boris Polyakov*

5

6   Institute of Solid State Physics, University of Latvia, Kengaraga street 8, Riga, Latvia, LV-1063

7

8   *e-mail: edgars.butanovs@cfi.lu.lv

9

10 Abstract

11   The development of nanoscale X-ray sensors is of crucial importance to achieve

12 higher spatial resolution in many X-ray-based techniques playing a key role in materials

13 science, healthcare, and security. Here, we demonstrate X-ray detection using

14 individual CdS, SnO$_2$, and ZnO nanowires (NWs). The NWs were produced via vapor-

15 liquid-solid technique and characterized using X-ray diffraction, scanning, and

16 transmission electron microscopy. Electrical measurements were performed under

17 ambient conditions while exposing two-terminal NW-based devices to X-rays

18 generated by a conventional tungsten anode X-ray tube. Fast and stable nanoampere-

19 range X-ray beam induced current (XBIC) in response to X-ray illumination was

20 observed. The high XBIC measured in the NW devices could be attributed to the

21 efficient transport and collection of generated charge carriers due to the single-

22 crystalline nature of NWs and the short NW length. Such fast-response and high-

23 sensitivity nanoscale X-ray detectors can find applications in sub-micron resolution

24 imaging and nanofocused beam shape measurements.

25

26 Keywords: *nanowire; X-ray detector; X-ray beam induced current; CdS; ZnO; SnO$_2$*

27

1. Introduction

Nanoscale X-ray sensors are key elements to achieve even higher spatial resolution in different X-ray based experiments, including imaging, diffraction, and spectroscopy. A decrease of the sensor size down to nanoscale is required for further advances in materials science, diagnostic and therapeutic healthcare, industrial process control and homeland security since many X-ray techniques are key research methods in these fields [1–3]. Nowadays, X-rays can already be focused down to sizes below 10 nm [4–6], while the conventional micron-scale direct-direction sensors lack the necessary resolution [7]. Typically, X-ray detection can be realized using indirect and direct methods, depending on how the radiation is transformed into a usable signal [8]. Indirect detection systems involve two steps which include X-ray conversion to visible light with a scintillator material and subsequent light detection via a pixelated sensor with photodiodes, in which the resolution is limited by the diffraction limit [9]. Direct detectors convert X-rays to an electrical signal directly that results in a significantly higher electrical signal per absorbed X-ray photon than in the previous case and are considered more preferable in a majority of hard X-ray detection applications [8]. There is still a demand for broadband, high sensitivity, and low-cost X-ray detectors, which operate at room temperature [1].

Conventional direct-detection semiconductor sensors are usually fabricated from bulk or thin-film materials, which makes further miniaturization and energy consumption reduction more sophisticated [10]. Amorphous Se is commonly used in mammography for low-energy X-ray beam detection, p-type Si finds applications for dose measurement and beam imaging, while high atomic number Z materials, such as Ge, GaAs, CdTe, and CdZnTe, are used at moderate and high X-ray energies, e.g., for security screening [1,8]. The working principle of such sensors is based on a conversion

2

of the absorbed X-ray photon energy to a readable electronic signal. An X-ray photon, when absorbed in the matter, creates a primary high-energy electron via the photoelectric effect, which subsequently gives its energy to the surrounding lattice to create an avalanche of secondary electron-hole pairs. Therefore, one absorbed X-ray photon can generate a large number of charge carriers that can be detected electronically. However, as the X-ray absorption is proportional to the volume of the material, conventional semiconductor X-ray detectors still have pixel dimensions in the order of tens of micrometers to obtain usable signal [7]. On the other hand, in devices based on nanostructured materials, which have smaller volume but very high crystalline quality and large surface-to-volume ratio, significantly more generated charge carriers per absorbed X-ray photon can be extracted than in bulk detectors [11].

During the last two decades one-dimensional (1D) semiconductor nanostructures, such as nanowires (NWs), have been extensively investigated for various applications in nanoelectronic and optoelectronic devices, such as transistors, photodetectors, and LEDs [12–14], because of their promising electrical and optical properties, which arise from the high surface-to-volume ratio and size confinement effects. The detection of light in the visible, infrared, and ultraviolet ranges using individual NW devices has been a particularly active research topic, mainly due to the high responsivity and fast response speed of single-crystal semiconductor NWs [15–18]. However, there are very few reports on X-ray beam induced current (XBIC) measurements in 1D semiconductor nanostructures. Ronning *et al.* have studied Ga/GaAs heterojunction embedded in a silicon NW with a SiO_2 shell in detail using a nanofocused X-ray beam and a combinatory approach [19] as well as demonstrated GaAs NW hard X-ray detection capability [20]. Wallentin *et al.* have extensively employed synchrotron radiation and the XBIC method together with X-ray

3

78 fluorescence and diffraction measurements in InP and InGaP NWs to study doping [21],

79 mechanical strain [22], charge carrier collection in single-NW solar cells [23], electrical

80 detection of X-ray absorption fine structure [24] and to develop a novel nanoscale

81 measurement technique for a beamline [25]. The same group of collaborators has also

82 demonstrated X-ray detection and beam shape characterization using individual NWs

83 either perpendicular [11] or parallel [26] to the X-ray beam propagation direction.

84 Furthermore, Li *et al.* have demonstrated X-ray detection using individual ZnCdTe

85 nanoribbons [27], while other studies only report the use of networked 1D

86 nanostructures [28,29]. Thus, for the development of novel efficient high-resolution X-

87 ray detectors based on NWs in the future, the detection of X-rays using NWs from

88 various semiconductor materials containing elements with different Z-numbers

89 deserves a more thorough study.

90   This study demonstrates the detection of X-ray radiation using individual CdS,

91 SnO_2, and ZnO NWs. Electrical measurements were performed under ambient

92 conditions while exposing two-terminal individual NW-based devices to soft X-rays

93 with continuous spectrum generated by a conventional X-ray tube with a tungsten

94 anode. The high nanoampere-range XBIC measured in the NW devices could mainly

95 be attributed to the efficient transport and collection of generated charge carriers due to

96 the single-crystalline nature of NWs and the short NW length. Such fast-response and

97 high-sensitivity nanoscale X-ray detectors might be useful for sub-micron resolution

98 imaging and nanofocused beam shape measurements.

99

100 2. Experimental section

101 2.1. Nanowire synthesis and characterization

4

102   CdS, SnO$_2$ and ZnO NWs were synthesized via atmospheric pressure chemical

103   vapor transport method in a horizontal quartz tube reactor. The NWs were grown on

104   oxidized silicon wafers SiO$_2$/Si(100) (*Semiconductor Wafer, Inc.*) coated with spherical

105   Au nanoparticles (NPs, *Alfa Aesar*, water suspension, 100 nm diameter) used as a

106   catalyst for the vapor-liquid-solid (VLS) mechanism.

107   *CdS NWs*: CdS powder (*98%, Alfa Aeasar*) was loaded in a ceramic boat and

108   placed in the center of the quartz tube, Au/Si substrates were placed downstream in a

109   lower temperature region. The reactor was heated to 875°C under a flow of N$_2$ carrier

110   gas and maintained for 20 minutes for the vapor transport and NW growth, followed by

111   natural cooling down to room temperature.

112   *SnO$_2$ NWs*: 0.3g of SnO:C=2:1 powder mixture was loaded in a ceramic boat in

113   the center of the quartz tube at 880°C, the vapor was transported downstream to the

114   Au/Si substrate at a lower temperature region using N$_2$ as a carrier gas. The temperature

115   during the growth was held constant for 90 minutes, followed by a natural cooling down

116   to room temperature.

117   *ZnO NWs*: 1:1 mixture of ZnO and carbon powders was loaded in a quartz tube

118   and kept at 950°C temperature for 90 minutes, followed by natural cooling down to

119   room temperature. The vapor was carried downstream to the Au/Si substrate by N$_2$ gas.

120   The phase of as-grown NWs was determined by X-ray diffraction (XRD) using

121   Rigaku MiniFlex 600 X-ray powder diffractometer with Bragg-Brentano θ-2θ

122   geometry and the 600W Cu anode (Cu Kα radiation, λ = 1.5406 Å) X-ray tube. NW

123   morphology was characterized using a scanning electron microscope (SEM, Lyra,

124   Tescan), while their inner crystalline structure was revealed using a transmission

125   electron microscope (TEM, Tecnai GF20, FEI) operated at a 200 kV accelerating

126   voltage.

127

2.2 Single nanowire two-terminal photodetector device fabrication and measurements

Two-terminal individual NW-based photodetectors were fabricated via the conventional photolithography technique. First, NWs were mechanically transferred to an oxidized silicon wafer (50 nm thick SiO_2), followed by spin-coating it with AZ1518 photoresist. The optical mask with the microelectrode pattern (5 μm gap between the electrodes) was aligned on top of a selected NW and exposed using the SUSS MicroTec MA/BA6 Gen4 mask aligner. A 10/100/70 nm thick Cr/Ag/Al film, respectively, was deposited via thermal evaporation method followed by a lift-off procedure. At least five NW-based photodetectors for each material were fabricated so consistent conclusions could be made.

Current−voltage ($I-V$) characteristics and photoresponse of the fabricated individual NW-based photodetector devices were measured with a low-noise current preamplifier (SR570, Stanford Research Systems) and oscilloscope (TDS2004B, Tektronix). Conventional water-cooled tungsten anode X-ray tube operated within 10-30 kV and 10-30 mA with 0.1 mm Be window was used as an X-ray source for NW illumination providing estimated X-ray photon flux of 10^9 ($1/s \cdot mm^2$). Spellman XLF60N1200/230 power supply is used to ensure stable lamp operation. Since the tube voltage was always below 30 kV, the *K*-characteristic lines of tungsten were never excited, and the X-ray spectrum included contributions from the multiple *L*-emission lines in the 7 keV–12 keV energy range and bremsstrahlung [30]. The schematic of the experimental setup is depicted in *Fig.1*. A 405 nm wavelength semiconductor diode laser (CNI Laser) with 0.5 W/cm^2 power was used for the optical photoresponse measurements. All the measurements were performed under ambient conditions.
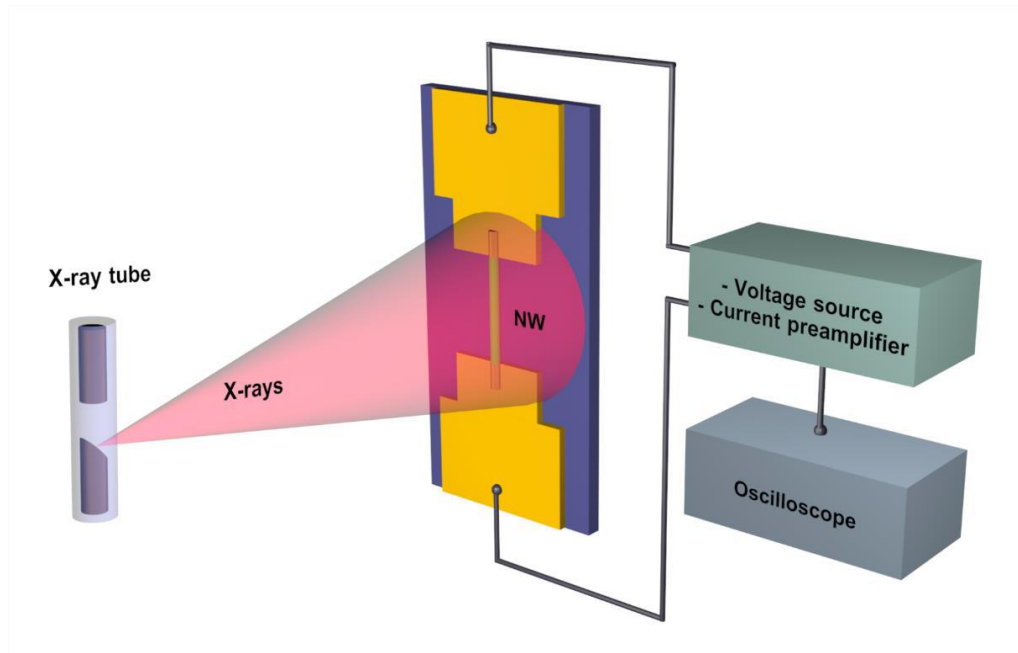
151

Figure 1. Schematic of the experimental setup. A single nanowire (NW) device on a Si/SiO$_2$ substrate was illuminated with X-rays, generated by a tungsten anode X- ray tube. X-ray beam induced current was measured by connecting the device to a low-noise current preamplifier and oscilloscope.

152

153   **3. Results and discussion**

154   The crystallographic structure and morphology of as-grown NWs are shown in

155   *Fig. 2*. SEM images of CdS, SnO$_2$, and ZnO NW arrays (*Fig. 2(a-c)*, respectively) show

156   smooth NWs with a length of 10 – 100 μm and a diameter of about 100 nm. To confirm

157   the presence of the respective phases in the as-grown NW samples, XRD measurements

158   were performed on the NW arrays on the Si(100)/SiO$_2$ substrates (see *Fig. 2(d)*). The

159   XRD patterns of each sample contain Bragg peaks of the desired highly-crystalline

160   phases: the pattern for CdS NWs was indexed to hexagonal wurtzite CdS structure

161   (ICDD-PDF #41-1049), SnO$_2$ NWs exhibit tetragonal cassiterite SnO$_2$ structure

162   (ICDD-PDF #41-1445), and the pattern of ZnO NWs corresponds to hexagonal wurtzite

163   ZnO structure (ICDD-PDF #36-1451). The Bragg peak at $2\theta \approx 33°$ is attributed to the

164   Si(100) substrate (forbidden Si(200) reflection). Furthermore, the results of XRD

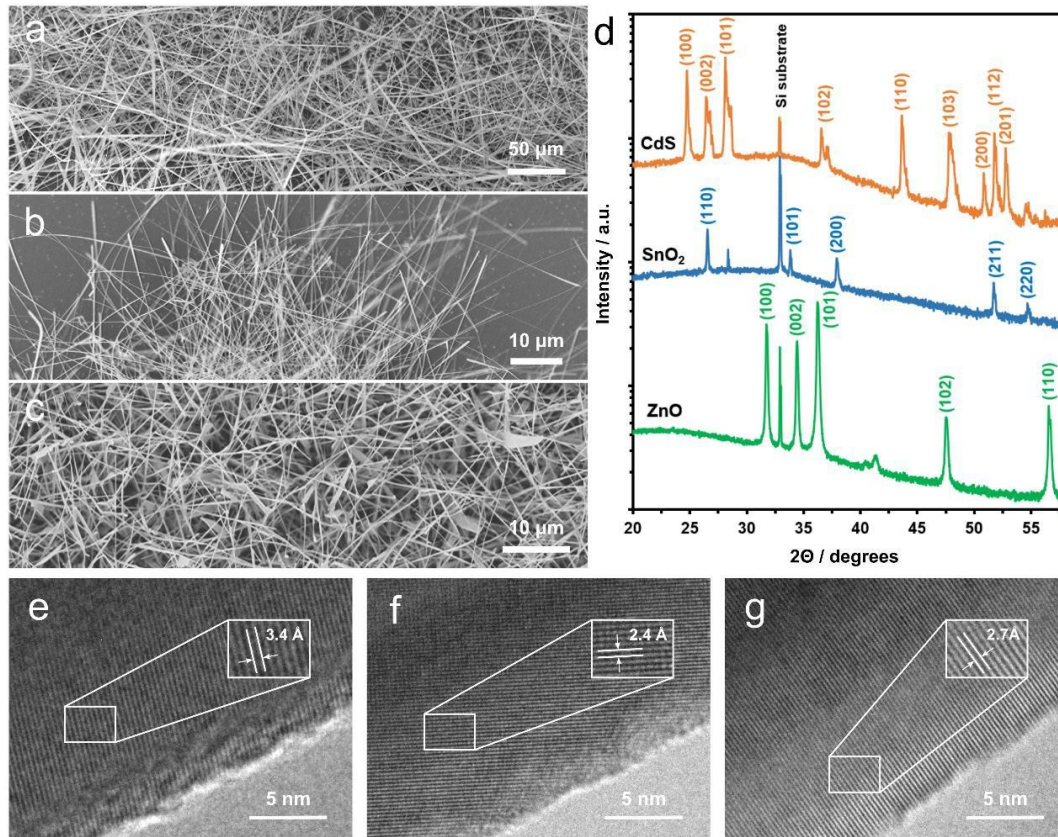7

Figure 2. Scanning electron microscope images of (a) CdS, (b) SnO_2 and (c) ZnO nanowires. (d) X-ray diffraction patterns of CdS, SnO_2, and ZnO nanowire arrays on Si(100)/SiO_2 substrates. Transmission electron microscope images of (e) CdS, (f) SnO_2, and (g) ZnO nanowires; the insets show the measured d-spacings.

165 measurements and the high-quality single-crystalline nature of the NWs were

166 confirmed by TEM studies (see *Fig. 2(e-g)*). Interplanar distances (d-spacings) in three

167 materials NWs measured for the resolved atomic planes are 3.4 Å (for CdS), 2.4 Å (for

168 SnO_2), and 2.7 Å (for ZnO) and are in good agreement with the lattice parameters given

169 in the corresponding ICDD-PDF files of hexagonal CdS (c=6.73 Å), tetragonal SnO_2

170 (a=b=4.74 Å) and hexagonal ZnO (c=5.20 Å).

171   The photoconductivity measurements were performed on two-terminal

172 individual NW-based devices produced using NWs transferred to Si(100)/SiO_2

173 substrates and conventional lithography technique. First, dark state current-voltage (I-

8

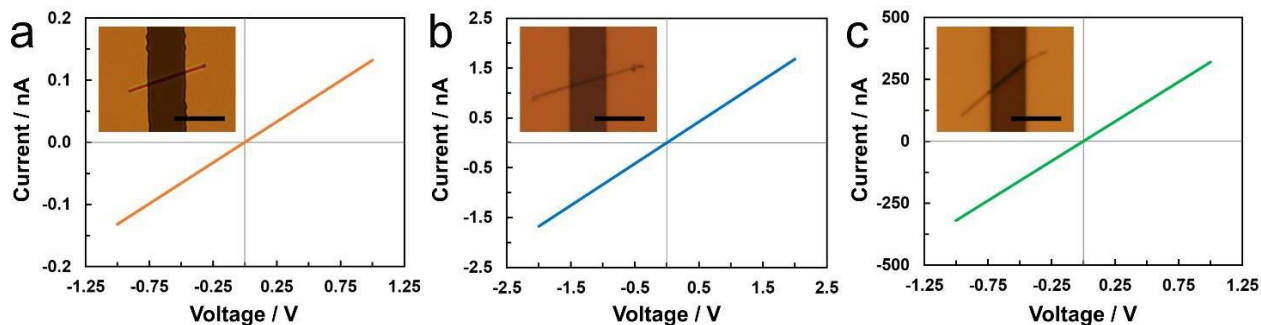174   V) characteristics of individual CdS, SnO_2, and ZnO NWs were measured (see *Fig.3*).

Figure 3. Dark state I-V characteristics of (a) CdS, (b) SnO_2, and (c) ZnO single- nanowire devices. Insets show optical microscope images of the nanowires lying on electrodes, scale bars correspond to 7 μm.

175 The I-V characteristics of all three materials exhibit linear behavior, indicating that the

176 ohmic contacts were formed between the NWs and the electrodes (chromium bottom

177 layer) [15,18,31], which is important for the efficient collection of photogenerated

178 carriers. CdS NWs exhibit a small dark current around 100 pA, the typical value for

179 SnO_2 NWs was around 1 nA, while ZnO NWs have a significantly higher dark current,

180 of the order of hundreds of nanoamperes. Note that semiconductor-based X-ray sensors

181 should have a low dark current to obtain a high signal-to-noise ratio, similarly to visible-

182 light photodetectors.

183 Next, the fabricated NW-based devices were illuminated with laser light with a

184 wavelength of 405 nm to check their photoconductive properties in the visible region

185 of light. The results of the time-dependent photocurrent measurements and

186 photodetector parameters are given in *Fig.S1* and *Table S1*. All NW-based devices

187 demonstrate very high spectral responsivity (up to 1429 A/W for SnO_2 NWs) and

188 external quantum efficiency with few μA large photocurrent, which is comparable to

189 similar *state-of-the-art* individual NW-based photoconductors [17,18,32,33]. The

190 response times (rise and decay) are around 150 ms for CdS and SnO_2 NWs, while ZnO

191 NWs typically exhibit slow response in a range of several seconds [17]. The slow

192 response speed and the high dark current of ZnO NWs can be altered by modifying

193   their surface, for example, with Au or PbI_2 which might also increase the X-ray

194   absorption of the nanostructures [34,35]. The excellent photodetection performance

195   (high photoconductive gain) indicates the high quality of the synthesized NWs and the

196   fabricated devices.

197   The as-fabricated individual NW-based devices were periodically exposed to

198   X-rays generated by a conventional tungsten anode X-ray tube at fixed tube voltage

199   (U_{tube}=30 kV) and current (I_{tube}=10 mA). X-ray photon flux was estimated to be around

200   10^9 (1/s·mm^2). *Fig.4(a-c)* shows the measured on/off photocurrent curves in individual

201   CdS, SnO_2, and ZnO NWs at different sample bias voltages. A stable increase of the

202   current in response to the X-ray illumination has been detected in all three cases. The

203   overshooting transient signal in *Fig.4(a)* can be attributed to charge trapping/de-

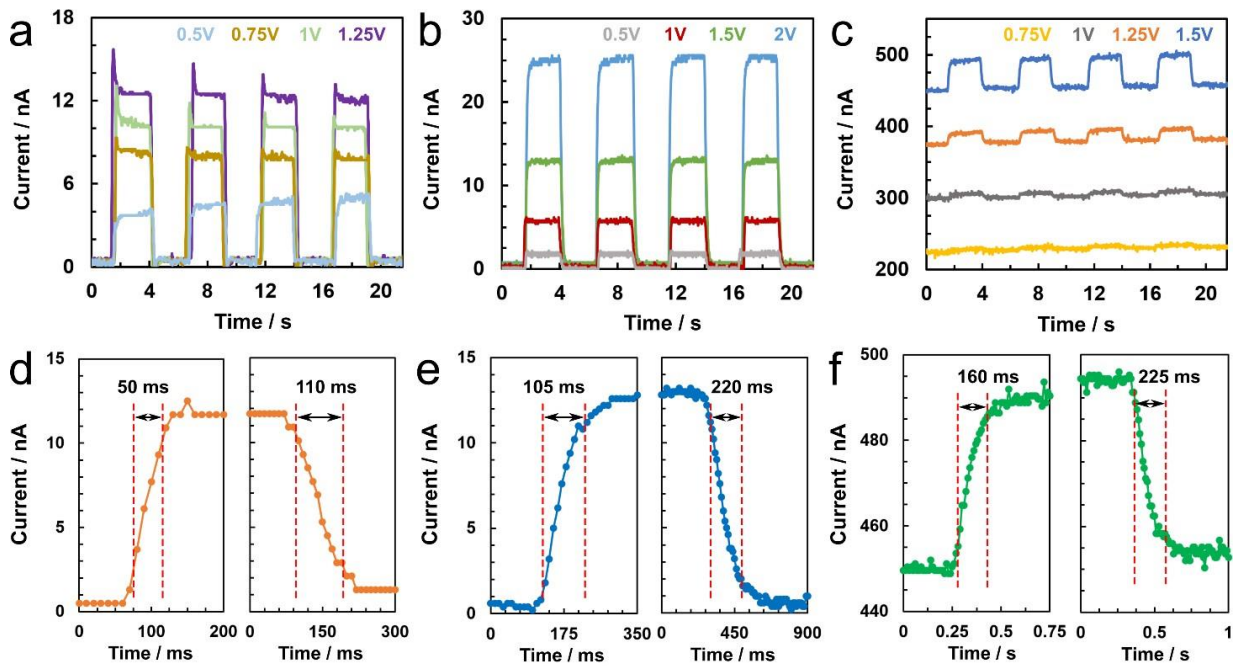204   trapping in semiconductor/electrode interfaces and to space-charge effects. Time-

Figure 4. On-off photoresponse to X-ray illumination at fixed tungsten anode X-ray tube voltage (30 kV) and current (10 mA) but different bias voltages, and the respective time-resolved graphs for (a,d) CdS, (b,e) SnO_2, and (c,f) ZnO single- nanowire devices.

11

205 resolved graphs in *Fig.4(d-e)* show the rise and decay rates of XBIC, the values being

206 in the range of 50-225 ms, which is sufficient for practical applications. The rise and

207 decay times are defined as the required time for the photocurrent to increase or decrease

208 to 90% or 10% of its maximum value, respectively. The magnitude of XBIC increases

209 proportionally to the applied bias voltage since the photogenerated charge carriers can

210 be collected more efficiently. High I_{on}/I_{off} ratios (up to around 100) were observed for

211 CdS and SnO_2 NWs, while it was very small for ZnO NWs (up to 1.1) due to its high

212 dark current. The measured XBIC is remarkably high, considering that the interaction

213 volume is significantly smaller than in conventional thin film or bulk pixelated X-ray

214 detectors. The high XBIC measured in the NW devices can mainly be attributed to the

215 efficient transport and collection of generated charge carriers due to the single-

216 crystalline nature of NWs and the short NW length. According to simplified

217 calculations of X-ray induced steady state conductance similar to Wallentin *et al.* [11]:

218 $G=q\mu N/l^2$, where G – conductance ($G=\Delta I/U$), q – electron charge, l – NW length, μ-

219 electron mobility, N – number of free electrons. For SnO_2 mobility $\mu=100$ cm^2/Vs

(CdS 220 $\mu=87$ cm^2/Vs, ZnO $\mu=220$ cm^2/Vs), $l=5\cdot10^{-4}$ cm, $\Delta I =10$ nA, U=1 V. For

$G=10^{-8}$ Ω^{-1}

221 we have N=156 electrons. On the other hand, number of X-ray induced steady state

222 carriers $N=\gamma\tau$, where γ - is carrier generation rate and τ - recombination lifetime. Carrier

223 generation rate $\gamma= p_{abs}\eta\Phi$, where p_{abs} – X-ray photon absorption probability, Φ - X-ray

224 flux, and η - number of electron-hole pairs generated per X-ray photon. If we assume

225 $p_{abs}\approx10^{-4}$, $\eta\approx10^4$, and $\Phi=1700$ ph/s, the carrier generation rate is $\gamma=1700$ s^{-1},

226 recombination lifetime is $\tau\approx10^{-1}$ s, then we obtain N=170 electrons, which is close to

227 the experimental value. Other effects, which arise from the NW size, such as charge

228 separation due to surface traps, photogating (influence of substrate) or photodoping

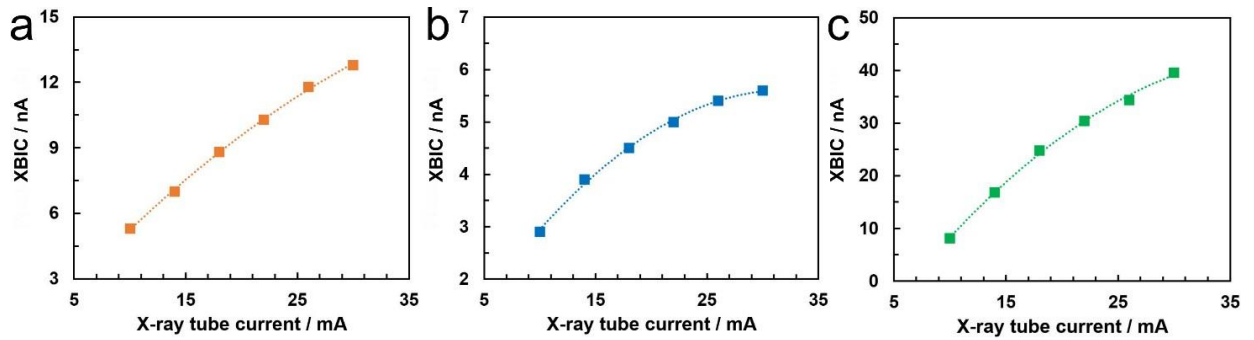229   [11], might play a role in the process, however, the significance of these factors should

Figure 5. X-ray beam induced current (XBIC) dependence on X-ray tube current at fixed bias (1 V for CdS, SnO_2 and 1.5 V for ZnO) and tube voltage (10 kV) for (a) CdS, (b) SnO_2, and (c) ZnO single-nanowire devices. The points are experimentally measured values and the dashed lines have been added for visual clarity.

230   be elucidated. Furthermore, no detectable temporary or permanent degradation of the

231   XBIC due to the exposure to X-rays over periods of several minutes was observed in

232   the NWs, demonstrating the stability needed for practical applications. Finally, since

233   relatively large areas of the samples were exposed to X-rays during the experiments, an

234   equivalent microelectrode pattern without any NW was also tested for comparison. An

235   electric signal around 100 pA was detected, which could be attributed to photoelectrons

236   emitted from the metal contacts [26] and leakage current through ionized substrate/air

237   gap; however, this signal does not contribute significantly to XBIC in NW-based

238   devices since it is orders of magnitudes smaller.

239   XBIC dependence on the X-ray tube current and voltage was also measured.

240   During the measurements, the current of the X-ray tube was varied between 10 mA and

241   30 mA, while the voltage (V_{tube}=10 kV) and device bias (U_{bias}=1 V for CdS, SnO_2 and

242   1.5 V for ZnO NWs) were kept constant. It can be seen in *Fig.5* that XBIC increases

243   strongly with the tube current in a sub-linear fashion. A similar relation was observed

244   when changing the tube voltage (see *Fig.S2*). Generally, an increase of the X-ray tube

245   current or voltage results in larger X-ray photon flux [30], i.e., more X-ray photons are

246   being generated, which leads to more absorbed photons in the NW in a unit of time,

14

247 subsequently giving larger XBIC. At the same time, when the voltage on the tube

248 changes, X-ray photons with higher energy are additionally generated, therefore, more

249 secondary electron-hole pairs are created per absorbed photon (higher yield of

250 photogenerated electron-hole pairs per X-ray photon), which again leads to a higher

251 XBIC. The reason for the sublinear dependence in *Fig.5* might be related to a decrease

252 in the charge carrier collection efficiency, since the high density of photogenerated

253 carriers at higher photon energies may influence the electrostatic potential distribution

254 in the NWs [26].

255

256 **4. Conclusions**

257 In this study, we demonstrated X-ray detection using individual CdS, SnO_2 and

258 ZnO nanowires, which were produced via vapor-liquid-solid technique and

259 characterized using X-ray diffraction, scanning and transmission electron microscopy.

260 Photocurrent measurements were performed under ambient conditions while exposing

261 two-terminal individual NW-based devices to X-rays generated by a conventional

262 tungsten anode X-ray tube.

263 X-ray beam induced current of tens of nanoamperes and a response rate in the

264 millisecond range were measured in the individual NWs, which is remarkably high,

265 considering that the interaction volume of NWs is significantly smaller than in

266 conventional thin film or bulk pixelated X-ray detectors. The high X-ray beam induced

267 current could mainly be attributed to the efficient transport and collection of generated

268 charge carriers due to the single-crystalline nature of NWs and the short NW length.

269 While X-ray detectors based on CdS and SnO_2 NWs exhibited a small dark current and

270 high on/off current ratio, a high dark current was measured in ZnO NWs, which limits

271 their applicability, however, that might be solved by modifying ZnO NW surface states.

15

272   Our study demonstrates that the possibilities of detecting X-rays using various

273   NWs and NW-based heterostructures containing high-Z element materials merit a more

274   thorough investigation. In the future, semiconductor NWs may enable the production

275   of novel high-resolution X-ray detectors, suitable for both synchrotron radiation,

276   especially nanofocused beams, and conventional X-ray tubes.

277

285

286

287

288   Supplementary information

289   Supplementary information is available and contains CdS, SnO_2, and ZnO

290   individual NW-based photodetector response measurements to visible (405 nm) light,

291   as well as a table containing spectral responsivity and external quantum efficiency

292   calculated for these devices. These same devices were used for the XBIC measurements

293   reported in the main text. XBIC dependance on X-ray tube voltage is also shown.

294

295   References

296   [1]   Thirimanne, H. M. *et al.* High sensitivity organic inorganic hybrid X-ray

16

297   detectors with direct transduction and broadband response. *Nat. Commun.* **9**,

298   2926 (2018)

299   [2]   Dinapoli, R. *et al.* EIGER: Next generation single photon counting detector for

300   X-ray applications. *Nucl. Instruments Methods Phys. Res. Sect. A Accel.*

301   *Spectrometers, Detect. Assoc. Equip.* **650**, 79–83 (2011)

302   [3]   Ballabriga, R. *et al.* The Medipix3RX: a high resolution, zero dead-time pixel

303   detector readout chip allowing spectroscopic imaging. *J. Instrum.* **8**, C02016–

304   C02016 (2013)

305   [4]   Mimura, H. *et al.* Breaking the 10 nm barrier in hard-X-ray focusing. *Nat. Phys.*

306   **6**, 122–125 (2010)

307   [5]   Chao, W., Harteneck, B. D., Liddle, J. A., Anderson, E. H. & Attwood, D. T.

308   Soft X-ray microscopy at a spatial resolution better than 15 nm. *Nature* **435**,

309   1210–1213 (2005)

310   [6]   Bajt, S. *et al.* X-ray focusing with efficient high-NA multilayer Laue lenses.

311   *Light Sci. Appl.* **7**, 17162–17162 (2018)

312   [7]   Denes, P. & Schmitt, B. Pixel detectors for diffraction-limited storage rings. *J.*

313   *Synchrotron Radiat.* **21**, 1006–1010 (2014)

314   [8]   Ballabriga, R. *et al.* Review of hybrid pixel detector readout ASICs for

315   spectroscopic X-ray imaging. *J. Instrum.* **11**, P01007–P01007 (2016)

316   [9]   Martin, T. & Koch, A. Recent developments in X-ray imaging with micrometer

317   spatial resolution. *J. Synchrotron Radiat.* **13**, 180–194 (2006)

318 [10] Luo, Z., Moch, J. G., Johnson, S. S. & Chen, C. C. A Review on X-ray Detection

319   Using Nanomaterials. *Curr. Nanosci.* **13**, 364–372 (2017)

320 [11] Wallentin, J. *et al.* Hard X-ray Detection Using a Single 100 nm Diameter

321   Nanowire. *Nano Lett.* **14**, 7071–7076 (2014)

17

322   [12]   Jia, C., Lin, Z., Huang, Y. & Duan, X. Nanowire Electronics: From Nanoscale

323   to Macroscale. *Chem. Rev.* **119**, 9074–9135 (2019)

324   [13]   Barrigón, E., Heurlin, M., Bi, Z., Monemar, B. & Samuelson, L. Synthesis and

325   Applications of III–V Nanowires. *Chem. Rev.* **119**, 9170–9220 (2019)

326   [14]   Yan, R., Gargas, D. & Yang, P. Nanowire photonics. *Nat. Photonics* **3**, 569–576

327   (2009)

328   [15]   Deng, K. & Li, L. CdS Nanoscale Photodetectors. *Adv. Mater.* **26**, 2619–2635

329   (2014)

330   [16]   Butanovs, E., Butikova, J., Zolotarjovs, A. & Polyakov, B. Towards metal

331   chalcogenide nanowire-based colour-sensitive photodetectors. *Opt. Mater.*

332   *(Amst).* **75**, 501–507 (2018)

333   [17]   Soci, C. *et al.* ZnO Nanowire UV Photodetectors with High Internal Gain. *Nano*

334   *Lett.* **7**, 1003–1009 (2007)

335   [18]   Hu, L., Yan, J., Liao, M., Wu, L. & Fang, X. Ultrahigh External Quantum

336   Efficiency from Thin SnO_2 Nanowire Ultraviolet Photodetectors. *Small* **7**, 1012–

337   1017 (2011)

338   [19]   Johannes, A. *et al.* In operando x-ray imaging of nanoscale devices:

339   Composition, valence, and internal electrical fields. *Sci. Adv.* **3**, eaao4044 (2017)

340   [20]   Zapf, M. *et al.* Hot electrons in a nanowire hard X-ray detector. *Nat. Commun.*

341   **11**, 4729 (2020)

342   [21]   Troian, A. *et al.* Nanobeam X-ray Fluorescence Dopant Mapping Reveals

343   Dynamics of in Situ Zn-Doping in Nanowires. *Nano Lett.* **18**, 6461–6468 (2018)

344   [22]   Wallentin, J., Osterhoff, M. & Salditt, T. In Operando X-Ray Nanodiffraction

345   Reveals Electrically Induced Bending and Lattice Contraction in a Single

346   Nanowire Device. *Adv. Mater.* **28**, 1788–1792 (2016)

347 [23] Chayanun, L. *et al.* Nanoscale mapping of carrier collection in single nanowire

348 solar cells using X-ray beam induced current. *J. Synchrotron Rad.* **26**, 102–108

349 (2019)

350 [24] Chayanun, L. *et al.* Spectrally resolved x-ray beam induced current in a single

351 InGaP nanowire. *Nanotechnology* **29**, 454001 (2018)

352 [25] Chayanun, L. *et al.* Combining Nanofocused X-Rays with Electrical

353 Measurements at the NanoMAX Beamline. *Crystals* **9**, 432 (2019)

354 [26] Chayanun, L., Hrachowina, L., Björling, A., Borgström, M. T. & Wallentin, J.

355 Direct Three-Dimensional Imaging of an X-ray Nanofocus Using a Single 60 nm

356 Diameter Nanowire Device. *Nano Lett.* **20**, 8326–8331 (2020)

357 [27] Li, S. *et al.* Synthesis and X-ray responsivity of $Zn_{0.75}Cd_{0.25}Te$ nanoribbons.

358 *Micro Nano Lett.* **6**, 624 (2011)

359 [28] Kim, J.-H. *et al.* A Novel X-Ray Radiation Sensor Based on Networked

360 SnO_2 Nanowires. *Appl. Sci.* **9**, 4878 (2019)

361 [29] Boucher, R. A., Bauch, J., Wünsche, D., Lackner, G. & Majumder, A. A

362 carbon nanotube based x-ray detector. *Nanotechnology* **27**, 475501 (2016)

363 [30] Boone, J. M., Fewell, T. R., Jennings, R. J., Molybdenum, rhodium, and

364 tungsten anode spectral models using interpolating polynomials with

365 application to mammography. *Med. Phys.* **24**, 1863–1874 (1997)

366 [31] Brillson, L. J. & Lu, Y. ZnO Schottky barriers and Ohmic contacts. *J. Appl. Phys.*

367 **109**, 121301 (2011)

368 [32] Zheng, D. *et al.* High-Performance Ferroelectric Polymer Side-Gated CdS

369 Nanowire Ultraviolet Photodetectors. *Adv. Funct. Mater.* **26**, 7690–7696

(2016)

370 [33] Yan, J. *et al.* High-performance solar-blind SnO_2 nanowire photodetectors

371 assembled using optical tweezers. *Nanoscale* **11**, 2162–2169 (2019)

372   [34]   Pescaglini, A. *et al.* Hot-Electron Injection in Au Nanorod–ZnO Nanowire

373   Hybrid Device for Near-Infrared Photodetection. *Nano Lett.* **14**, 6202–6209

374   (2014)

375   [35]   Butanovs, E., Piskunov, S., Zolotarjovs, A. & Polyakov, B. Growth and

376   characterization of PbI_2-decorated ZnO nanowires for photodetection

377   applications. *J. Alloys Compd.* **825**, 154095 (2020)

378

379   **Table of Contents/Abstract graphic:**

380
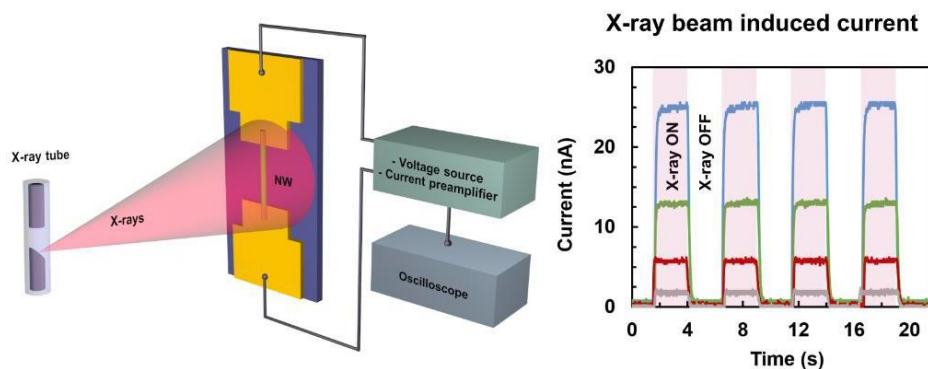
Author credit statement

Edgars Butanovs: Methodology, Validation, Investigation, Visualization, Writing - Original Draft. **Aleksejs Zolotarjovs:** Investigation. **Alexei Kuzmin:** Conceptualization, Writing - Review & Editing. **Boris Polyakov:** Conceptualization, Supervision, Investigation, Writing - Review & Editing.